



## Supplementary Material for

### Measuring magnetic field texture in correlated electron systems under extreme conditions

King Yau Yip\*, Kin On Ho\*, King Yiu Yu\*, Yang Chen, Wei Zhang, S. Kasahara, Y. Mizukami, T. Shibauchi, Y. Matsuda, Swee K. Goh†, Sen Yang†

\*These authors contributed equally to this work.

†Corresponding author. Email: skgoh@cuhk.edu.hk (S.K.G.); syang@cuhk.edu.hk (S.Y.)

Published 13 December 2019, *Science* **366**, 1355 (2019)  
DOI: 10.1126/science.aaw4278

#### This PDF file includes:

Materials and Methods  
Supplementary Text  
Figs. S1 to S19  
Tables S1 and S2  
References

## CONTENTS

1. Materials and Methods	2
A. Pressure cell design	2
B. The sample and the diamond particles	2
C. Experimental setup	4
D. Spatial resolution	5
E. Size comparison between diamond particles and vortices	6
2. Determine the physical parameters from the ODMR spectrum	6
A. Pressure calibration	8
1. By the optical spectrum of ruby	8
2. By ODMR	8
3. Mapping pressure gradient with NV centers	11
B. Determine the magnitude and orientation of the magnetic field	13
1. Determine the magnetic field relative to NV center axis	13
2. Determine the magnetic field relative to the sample $c$ -axis	18
3. AC susceptibility measurements	21
4. Optimizing the ODMR pulse sequence by examining the thermal load from the measurements	22
5. The diamagnetism associated with superconductivity measured via nanodiamonds	23
6. Determining the ambient pressure $T_c$ via AC susceptibility and resistivity measurements	25

## 1. MATERIALS AND METHODS

### A. Pressure cell design

The schematic of the interior of the pressure cell is shown in the main text Figure 1(A,B) [26, 34]. The pressure cell consists of a pair of opposing moissanite anvils. Glycerin was used as the pressure transmitting fluid. High-pressure AC susceptibility measurements were conducted via a mutual inductance technique with the larger coil on the gasket as the modulation coil and the microcoil as the pick-up coil. The modulation coil with  $\sim 150$  turns was placed around the anvil outside the pre-indented region of the gasket, and the modulation frequency was 12.471 kHz. The pickup coil of 7.5 turns with a diameter of  $200\text{ }\mu\text{m}$  was placed directly inside the gasket hole, which together with the anvils form the high-pressure chamber. The microcoil also served as an effective source of microwave for spin resonance experiments. The opening on the cell body allows the optical access for both optical excitation and fluorescence collection purposes. The effective numerical aperture is around 0.1. The pressure of the cell is calibrated by two methods, namely the ESR spectrum shift of crystal field of NV centers and the optical spectrum shift of  $\text{Cr}^{3+}$  line in a  $40\text{ }\mu\text{m}$  size ruby inside the high pressure chamber. More details on the two methods are presented in Section 2A.

### B. The sample and the diamond particles

The  $\text{BaFe}_2(\text{As}_{0.59}\text{P}_{0.41})_2$  sample used in this study has a shape of an irregular pentagon, with the length of each side ranging from  $80\text{ }\mu\text{m}$  to  $100\text{ }\mu\text{m}$ , as shown in Fig. 1B in the main text. The thickness is  $80\text{ }\mu\text{m}$ .

Single crystalline diamond particles with the average size of  $1\text{ }\mu\text{m}$  and the nitrogen concentration of 3 ppm are from Adámas Nanotechnologies. The diamond particles were spread on the surface of the sample, which is placed inside the pickup coil. The number of NV centers in each diamond particle is on the order of 1 million.

Generally, the gasket hole can move under pressure, this will result in relative shifts between the anvils and the sample during pressure changes. Here, diamond particles were spread directly on sample surface. We have checked if there is either shift or rotation of diamond particles relative to the sample during pressure or temperature changes.

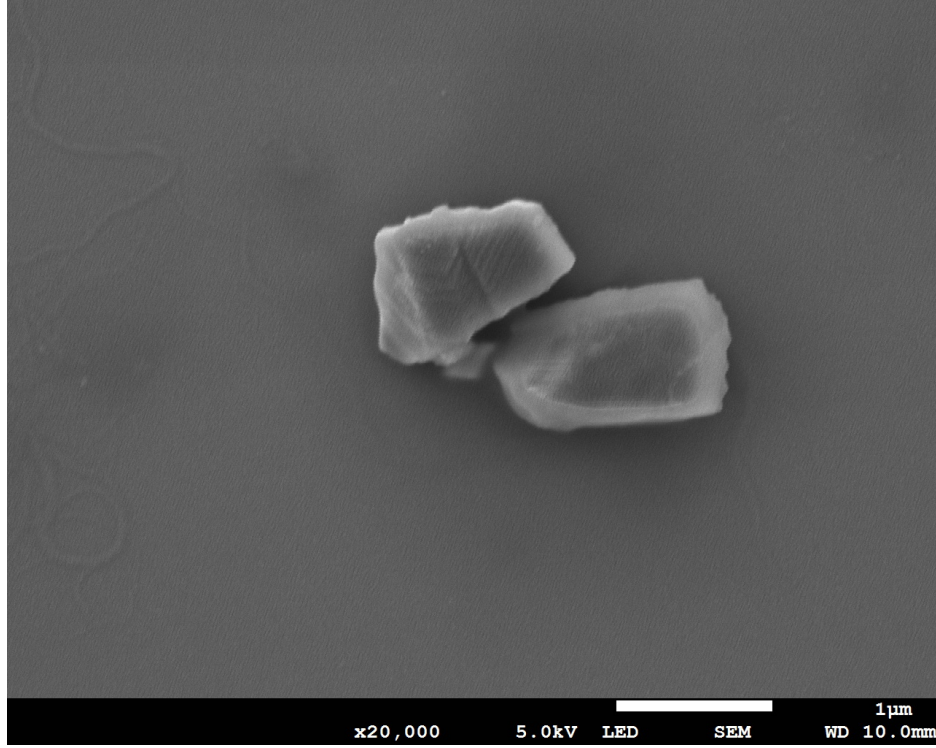


FIG. S1. **SEM image of  $1\mu\text{m}$  diamond particles** The diamond particles are the same type as the ones used in this study.

We compared confocal images for different pressures and temperatures and calculated the relative distances. Within our optical spatial resolution, which is a few microns, we did not observe any shift of diamond particles on the sample surface.

We repeated the measurements for each diamond particle for several times and measured the temperature dependence for different thermal duty cycles. The data are reproducible (e.g. Section 4 below). We also compared the angle between the applied magnetic field direction (which is along the c-axis of the sample) and the NV axis for different pressures, but observed no noticeable change. In fact, since we calibrate the angle of diamond particle relative to the sample at each pressure point, even if there is a rotation during pressure changes, it will not influence our results.

One possible explanation for the spatial stability of the diamond particles can be seen from the SEM image in Fig. S1. These particles are more like slabs/flakes than spheres. Under strong Van der Waals force, they stick well on the sample surface.

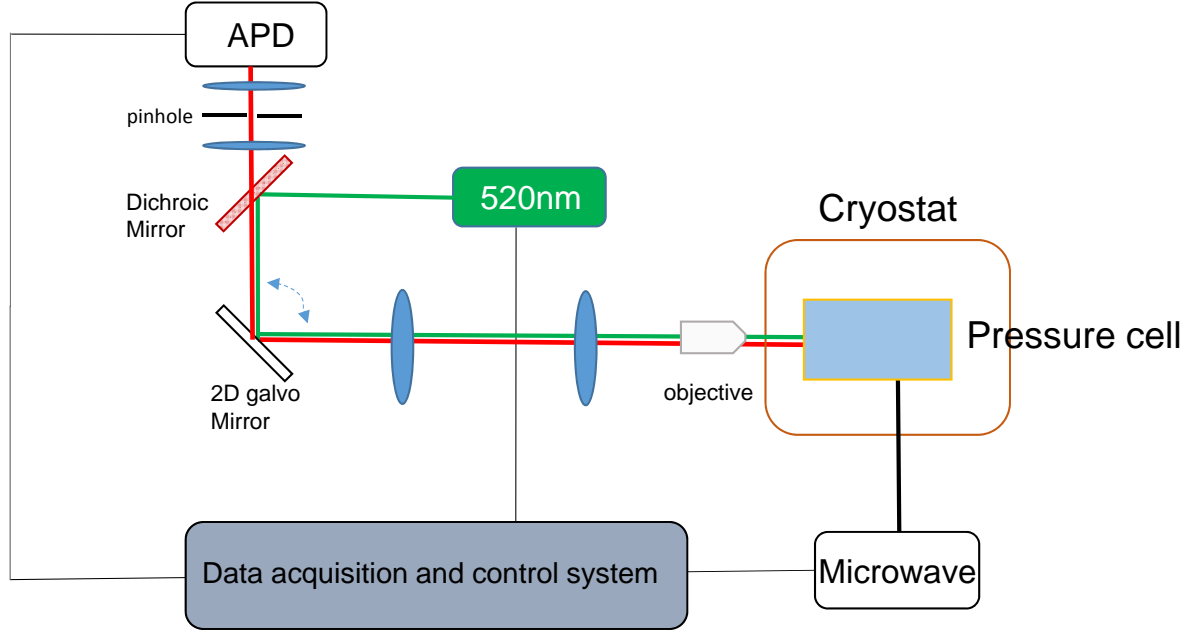


FIG. S2. Schematic drawing of the optical confocal microscope setup

### C. Experimental setup

The experimental platform is a home-made optical confocal setup based on Montana Instruments Cryostation (Fig. S2). The pressure cell is installed on the cold finger with a temperature sensor next to the cell body. The base temperature measured from this sensor is around 6.5 K. The laser excitation is provided by a 520 nm laser diode. The phonon side band is detected by Perkin-Elmer avalanche photodiodes (APDs). Microwave source is Rohde & Schwarz SMIQ signal generator. The circuit diagrams for AC susceptibility and ODMR measurements are shown in Fig. S3.

To perform the experiment, the sample was first cooled down to the base temperature ( $\sim 6.5$  K) without an external magnetic field. At the base temperature, a magnetic field was applied along the  $c$ -axis of the sample by a permanent magnet to prepare for the ODMR measurements as a function of temperature.

The pulse sequence of ODMR is shown in Figure 2A of the main text. Both the laser power and the microwave power were carefully tuned so that they do not introduce heating. The wait time  $t_{\text{wait}}$  between two consecutive pulses further minimizes the heating. To verify that our signals are not compromised by any unwanted heating, measurements of the

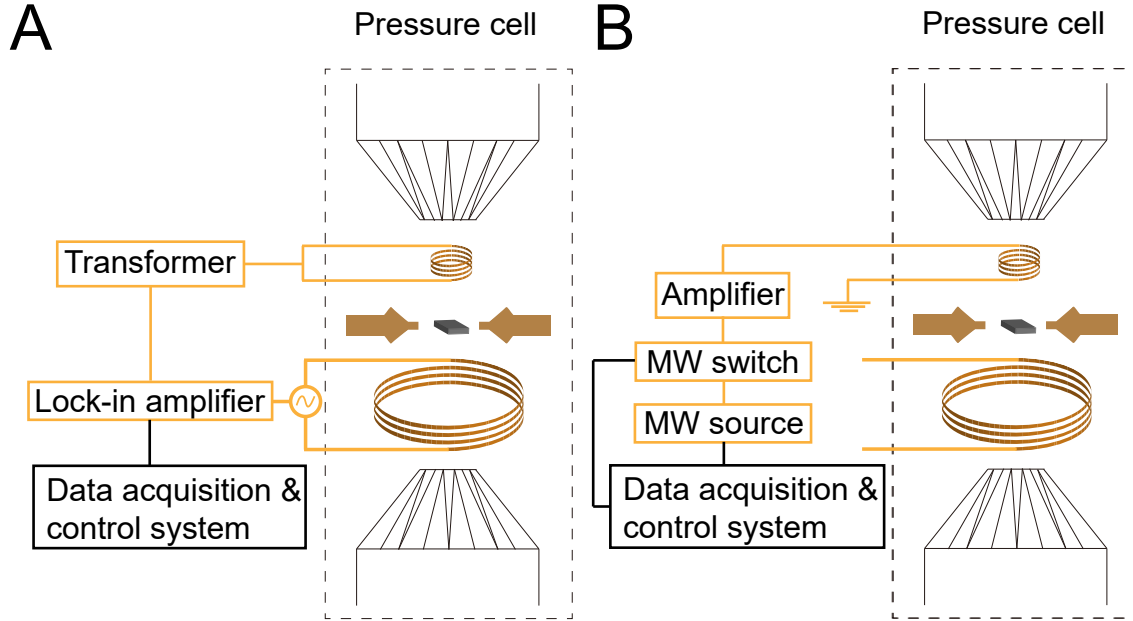


FIG. S3. **Circuit diagrams for AC susceptibility measurements (A) and ODMR measurements (B).** Inside the pressure cell, between two anvils, from the top to the bottom: microcoil, sample surrounded by a metal gasket, the larger coil that serves as the driving coil for AC susceptibility.

superconducting transition with different  $t_{\text{wait}}$  were conducted and presented in Section 5. The perfect agreement of the experimental curves for different  $t_{\text{wait}}$  rules out the existence of the heating effect.

#### D. Spatial resolution

The spatial resolution is limited by both the size of diamond particles we use and the diffraction resolution limited by the numerical aperture ( $N.A.$ ) of the pressure cell. The  $N.A.$  of our pressure cell is around 0.1 which leads a spatial resolution in the order of microns. However, by using particles smaller than this limitation, we can reach a better spatial resolution. Therefore, in our approach, the spatial resolution is the size of diamond particles we use. We have successfully used nanodiamonds of size 140 nm to demonstrate the diamagnetism associated with superconductivity with the same protocol (see details below). Since nanodiamonds with a size of around 10 nm and good spin properties are available, we

can in principle push the spatial resolution to sub-100 nm.

### E. Size comparison between diamond particles and vortices

The lattice constant  $a_V$  of the vortex lattice can be estimated by  $a_V \sim \sqrt{\frac{20.7 \text{ G}\mu\text{m}^2}{B}}$ . The size of the diamond particles we use here is around  $1 \mu\text{m}$ . Since the minimum magnetic field we use is above 40 G,  $a_V$  is less than  $0.7 \mu\text{m}$ . Thus,  $a_V$  is less than the typical size of our sensor and what we have observed is the average effect of several vortices.

## 2. DETERMINE THE PHYSICAL PARAMETERS FROM THE ODMR SPECTRUM

The relevant quantities we aim to detect in this study are the magnetic field and the pressure, which can be achieved through the measurement of the ESR spectra of the NV center.

Nitrogen vacancy center consists of a nitrogen atom replacing a carbon atom and a vacancy nearby. Throughout this study, the NV centers are in the negatively charged state, i.e. the  $NV^-$  center, which has an electron spin 1. The crystal axis between the nitrogen atom and vacancy defines the NV center axis. There are 4 possible orientations in a single crystal diamond. Due to the large crystal-field-induced zero field splitting (2.87 GHz in ambient condition), under a weak magnetic field, the NV center's quantization axis, which is conventionally called the z-axis, is along its defect axis, i.e. the  $C_{3v}$  symmetry axis, shown in Fig. S4.

Thus, the Hamiltonian of the NV center can then be written as:

$$H = D \left[ S_z^2 - \frac{S(S+1)}{3} \right] + \gamma \vec{B} \cdot \vec{S} + E(S_x^2 - S_y^2), \quad (\text{S1})$$

where  $D$  is the longitudinal component of the zero field splitting, determined by both the temperature and the pressure. Therefore, our NV centers also works as an *in-situ* pressure sensor.  $E$  is the transverse component and works as the indicator of strain. Below 70 kbar, we observed no significant change of  $E$ . The second term is the Zeeman term. In the reference frame of the NV center, the longitudinal component along the NV center axis  $\gamma B_z S_z$  of the  $\gamma \vec{B} \cdot \vec{S}$  term leads to the Zeeman splitting (here  $B_z = B_{Long}$ ); the transverse component  $\gamma(B_x S_x + B_y S_y)$  causes an overall frequency shift [37]  $\Delta\varepsilon \sim \frac{\gamma^2(B_x^2 + B_y^2)}{D} = \frac{\gamma^2 B_{Trans}^2}{D}$ .

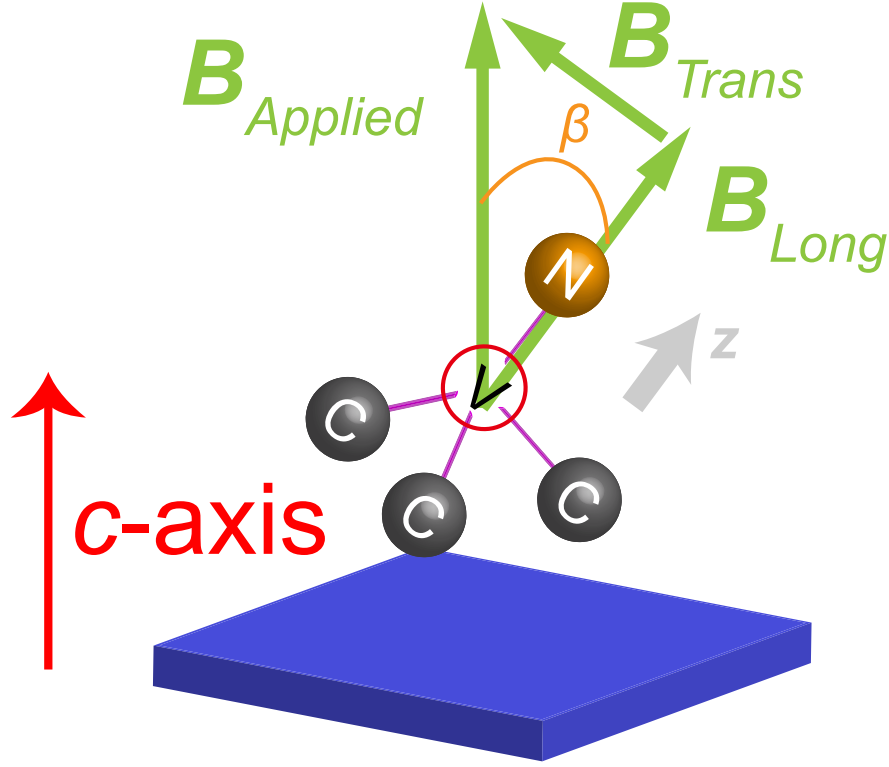


FIG. S4. **Schematic drawing of two reference frames in this study: the sample frame and the NV center frame.** The  $c$ -axis is the stacking direction of the FeAs planes of the sample. The applied magnetic field is always parallel to the sample  $c$ -axis in this study. Diamond particles are randomly oriented relative to the sample frame. The NV center's quantization axis, which is conventionally called the  $z$ -axis, is along its defect axis.

A more precise calculation can be found in [38]. The transverse term mixes the states from  $|0\rangle, |\pm 1\rangle$  to a new basis  $|0\rangle, |\pm\rangle$ . The transition frequencies  $f^\pm$  of  $|0\rangle \Leftrightarrow |\pm\rangle$ , up to the second order perturbation, can then be described as:

$$f^\pm = D + \frac{3\gamma^2 B^2}{2D} \sin^2 \beta \pm \gamma B \cos \beta \sqrt{1 + \frac{\gamma^2 B^2}{4D^2} \tan^2 \beta \sin^2 \beta}, \quad (\text{S2})$$

where  $B = \sqrt{B_{Long}^2 + B_{Trans}^2}$ ,  $B_{Trans} = \sqrt{B_x^2 + B_y^2}$  and  $\tan \beta = B_{Trans}/B_{Long}$ .

The relative angle  $\beta$  between the magnetic field and the NV center axis can then be inferred from the transition frequencies.



## A. Pressure calibration

The applied pressure is calibrated via two methods: by the optical spectrum of ruby at room temperature and the ODMR spectrum at low temperature.

### 1. By the optical spectrum of ruby

Ruby is chromium doped  $\text{Al}_2\text{O}_3$ . The optical spectrum of  $\text{Cr}^{3+}$  near 694 nm contains two resonances: R1 and R2. Both transition frequencies are sensitive to the temperature (0.068 Å/K) and the pressure (0.364 Å/kbar) [39]. Ruby fluorescence spectroscopy has become the standard way of determining pressure in pressure cells [40].

The calibration of the pressure was first carried out by measuring ruby fluorescence at room temperature. Fig. S5 shows the ruby fluorescence from  $p_1$  to  $p_8$  (see also Fig. 3B of the main text). The indices indicate the chronological order of the pressure application. At 34.9 kbar ( $p_5$ ),  $T_c$  of our sample is too low for a meaningful ODMR experiment. Therefore, we decreased the pressure to 15.0 kbar ( $p_6$ ), 7.5 kbar ( $p_7$ ) and 8.3 kbar ( $p_8$ ), enabling the collection of  $H_{c1}$  and  $H_{c2}$  data shown in the main text. In addition, the absence of the broadening of R1 peaks reflects the superior hydrostatic condition of our pressure environment throughout the entire experiment.

### 2. By ODMR

The Hamiltonian of the NV center without a magnetic field can be written as:

$$H = D \left[ S_z^2 - \frac{S(S+1)}{3} \right] + E(S_x^2 - S_y^2). \quad (\text{S3})$$

$D$  is the longitudinal component of the zero field splitting due to the local electric field induced by the defect. It is sensitive to changes of the lattice constant as well as the distortion of the lattice. Thus it can be used to sense both the temperature change and the pressure applied. When temperature is above 250 K,  $dD/dT = -74.2$  kHz/K; when temperature is below 30 K, there is nearly no change of  $D$  versus temperature [41]. On the other hand, the pressure sensitivity is around  $dD/dP = 1.46$  MHz/kbar [16]. At zero magnetic field,  $D$  can be determined from the overall shift of the ODMR spectrum.

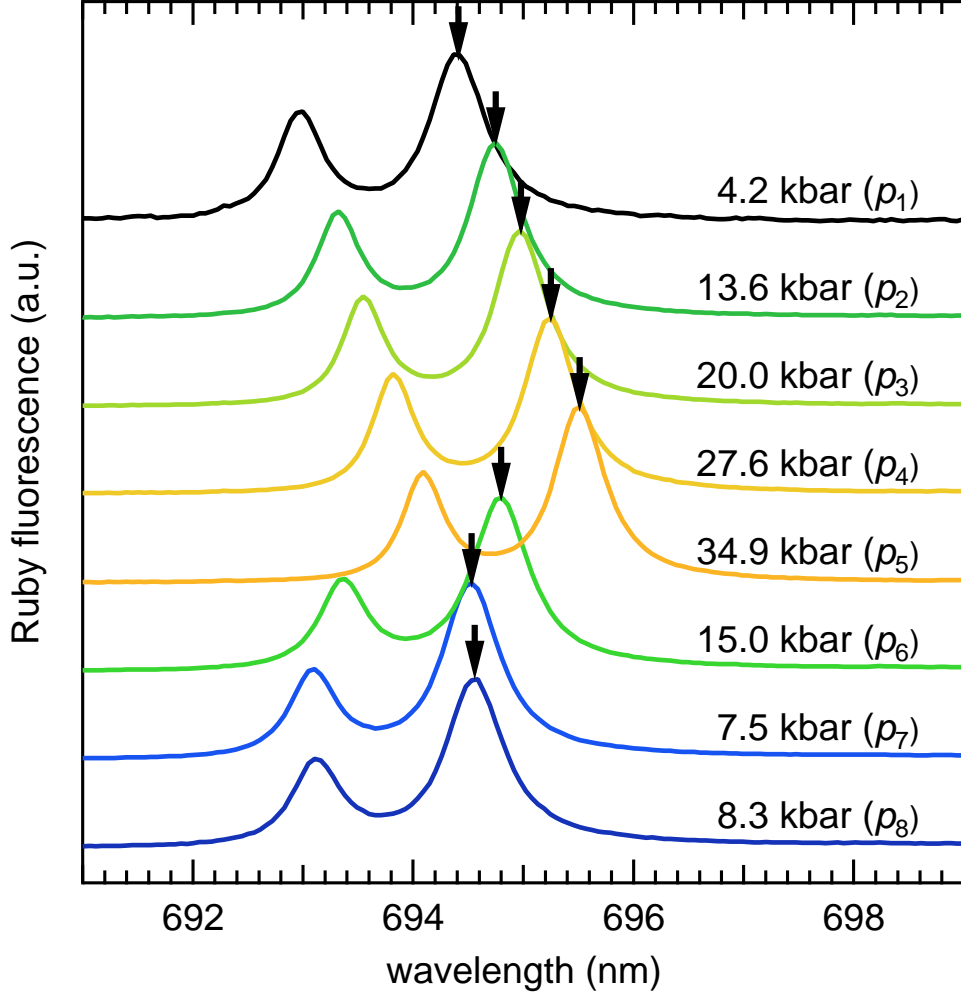


FIG. S5. Ruby fluorescence for each of the pressure point measured at room temperature in the order of  $p_1$  to  $p_8$ . The R1 peaks for pressure determination are annotated with the arrows.

It is possible to distinguish the temperature and pressure from the spectrum. At room temperature,  $D$  under certain temperature can be calibrated when there is no pressure applied. In fact, above 350 K, the difference between the temperature dependence and pressure dependence is near 1000 times. Unlike the calibration with ruby, a slight change of the temperature will not influence the pressure calibration too much. Thus, ODMR offers an avenue to determine the pressure with a much higher accuracy.

Several groups have demonstrated this method by using NV centers in bulk diamond [16, 21]. The pressure has been measured up to 60 GPa/600 kbar. Since we use diamond particles

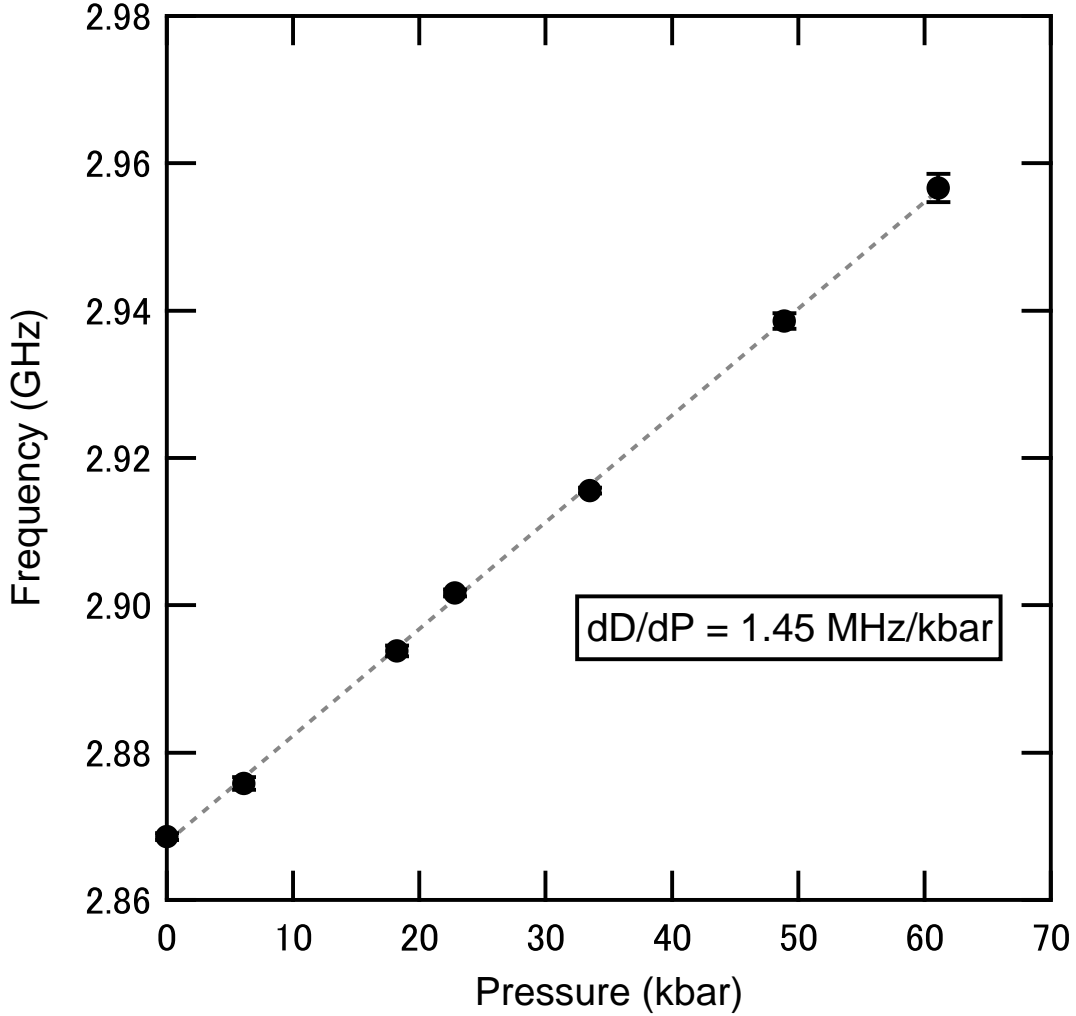


FIG. S6. **The change of  $D$  versus pressure applied in room temperature.** The pressure is measured by the ruby fluorescence spectroscopy.

that are mixed with the pressure transmitting fluid, the first step is to calibrate the pressure sensitivity compared with the bulk diamond sample. We performed this measurements by using nanodiamonds with an average size of 100 nm and 500 NV centers per particle. The pressure measured by ODMR is calibrated against the ruby results, as shown in Fig. S6. Our results show that the pressure dependence of  $D$ ,  $dD/dP$ , in nanodiamonds is 1.45 MHz/kbar, which agrees nicely with the results obtained for bulk diamonds [16].

With  $dD/dP$  established, we can measure the pressure of our cell *in-situ* at low temperatures. We choose 30 K as the temperature at which we measure the pressure. The pressure values determined at 30 K are used throughout the main text.

Since NV center is a point defect with a small size, this method can detect the local pressure distributions. In this experiment, due to the properties of the sample, we did not need pressure beyond the hydrostatic condition of the pressure transmitting fluid (glycerine). Therefore, the pressure measured shows the same value everywhere, and the ODMR spectrum linewidth does not vary spatially. However, when pressure goes beyond the hydrostatic limit of a given pressure transmitting fluid, there will be a pressure gradient in the pressure medium. The ODMR method will be able to reveal this distribution, and correlate the pressure distribution to local quantum phase of the sample.

### *3. Mapping pressure gradient with NV centers*

Because diamond particles are immersed in the pressure medium, they can be used to monitor the pressure distribution in the pressure medium. This is quite important because, depending on the pressure strength, the pressure medium can go from hydrostatic condition, where the pressure is uniform and isotropic, to non-hydrostatic. The non-uniformity in the non-hydrostatic condition can influence the bulk response of the sample. NV centers give a unique opportunity to map the distribution with a high spatial resolution. Non-hydrostatic pressure can lead to two effects on NV centers: the non-uniform distribution of the pressure over distance, and the broadening of the spectrum line.

The change of the ODMR linewidth is a good indicator for this freezing effect. In general, inhomogeneity due to non-hydrostatic medium can lead to spectrum broadenings in resonance type experiments. Indeed, various groups have used the linewidth changes as such an indicator, see for example Ref. [42, 43].

To detect the onset of the pressure inhomogeneity, we measure both the ODMR spectra and, as a benchmark, the ruby fluorescence spectra. The diamond particles have a typical size of  $1\text{ }\mu\text{m}$ , while the ruby particles have a typical size of  $40\text{ }\mu\text{m}$ . To illustrate the principle, we show a separate set of data on 98.5% pure glycerine without the superconductor. Note that in all other experiments in this study, we use 99.5% pure glycerine. With 98.5% pure glycerine, the critical pressure, above which the pressure medium becomes inhomogeneous, is reduced.

In Fig. S7, we show both the ODMR linewidth and ruby fluorescence linewidth. For both datasets, the linewidth appears to increase more rapidly above  $\sim 35\text{ kbar}$ . Hence, we

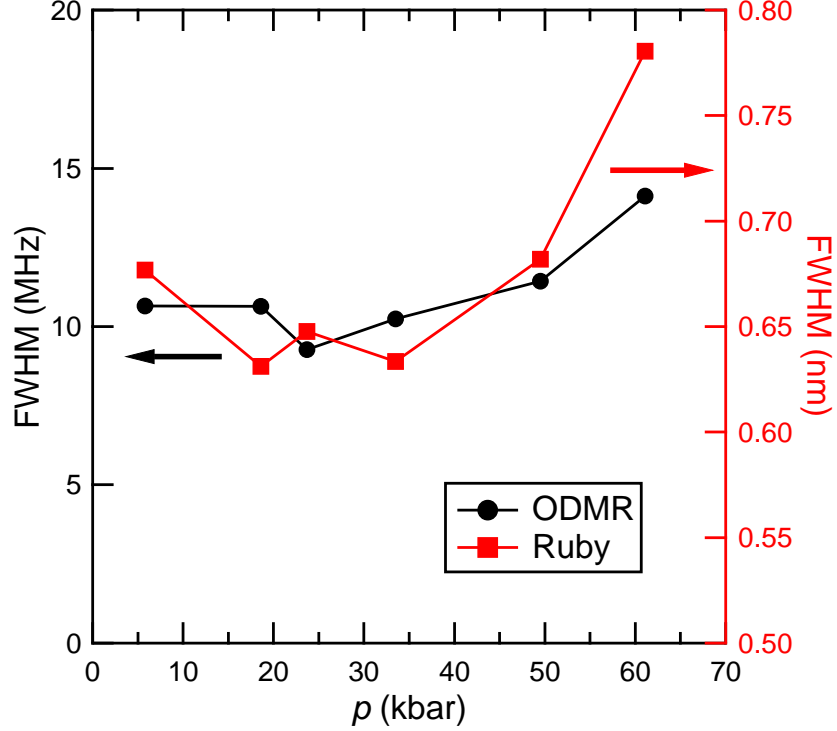


FIG. S7. The ODMR linewidth of NV centers (black) and the linewidth of optical spectra of ruby (red) in 98.5% pure glycerine against pressure. ODMR spectra were measured with the same power for both microwave and excitation laser, and the linewidth is averaged over 5 diamond particles.

can conclude that for 98.5% pure glycerine, the medium remains hydrostatic up to at least 35 kbar. To confirm the presence of the pressure inhomogeneity, we present the spatial dependence of pressure values at an average pressure of 59.7 kbar. A variation up to  $\pm 5\%$  has been detected, as shown in Fig. S8.

As a corollary, with the purer 99.5% glycerine, this critical pressure will be even higher. In the main text, all data were taken with 99.5% pure glycerine. We processed the ODMR data taken at 30 K from Fig. 3 in main text and the ruby spectra from Fig. S5. The pressure dependence of the linewidths is shown in Fig. S9. There is no broadening effect up to 34.9 kbar. This means all results were taken in hydrostatic region.

It was reported in Ref. [42] that glycerine's critical pressure is 1.4 GPa (=14 kbar). However another later paper [43] obtained a critical pressure which was much higher ( $>35$  kbar). Both papers used 99.5% pure glycerine. Our results agree better with the results of Ref. [43].

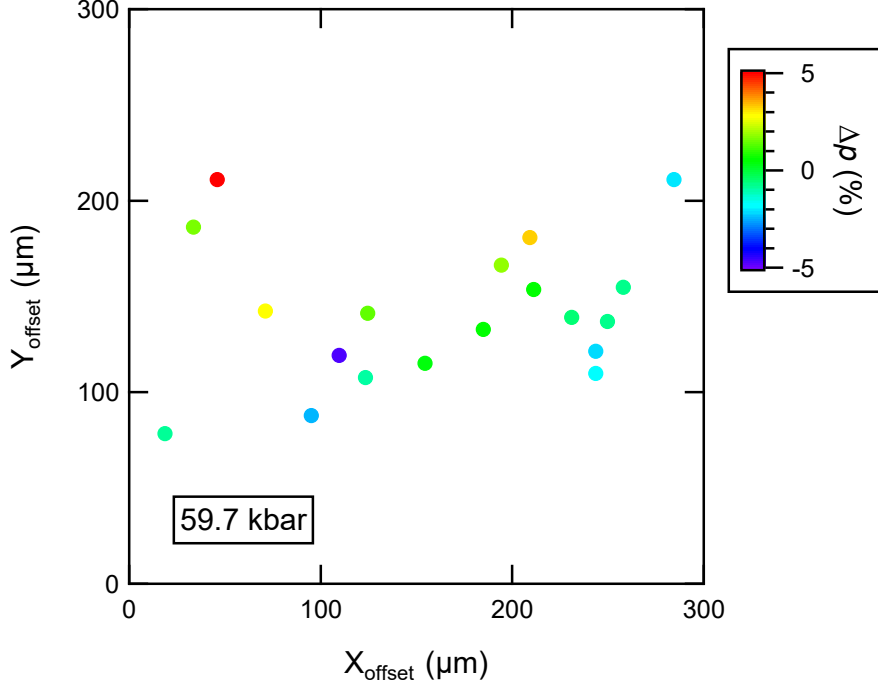


FIG. S8. The pressure distribution measured by NV centers in 98.5% pure glycerin at an average pressure of 59.7 kbar.

The difference is interesting and we speculate that it may spring from the different preparation process, which might affect the actual purity.

To summarize, our data in this section show this study was done in hydrostatic condition. These data also demonstrate the potential utility of NV centers for mapping the pressure distribution in a pressure medium with high spatial resolution, a fact that should be of interest to the high pressure community.

## B. Determine the magnitude and orientation of the magnetic field

### 1. Determine the magnetic field relative to NV center axis

In this section, we will consider the Zeeman term  $\gamma \vec{B} \cdot \vec{S}$  of Eqn. S1 in the reference frame of the NV center as shown in Fig. S4. Gyromagnetic ratio is  $\gamma/2\pi = 2.8$  MHz/G. The Zeeman term has the longitudinal component  $\gamma B_z S_z$  and transverse component  $\gamma(B_x S_x + B_y S_y)$  relative to the NV center quantization axis, i.e. the defect axis. As shown in Section 2, the longitudinal component will split the energy of  $S_z = +1$  and  $S_z = -1$  by the Zeeman

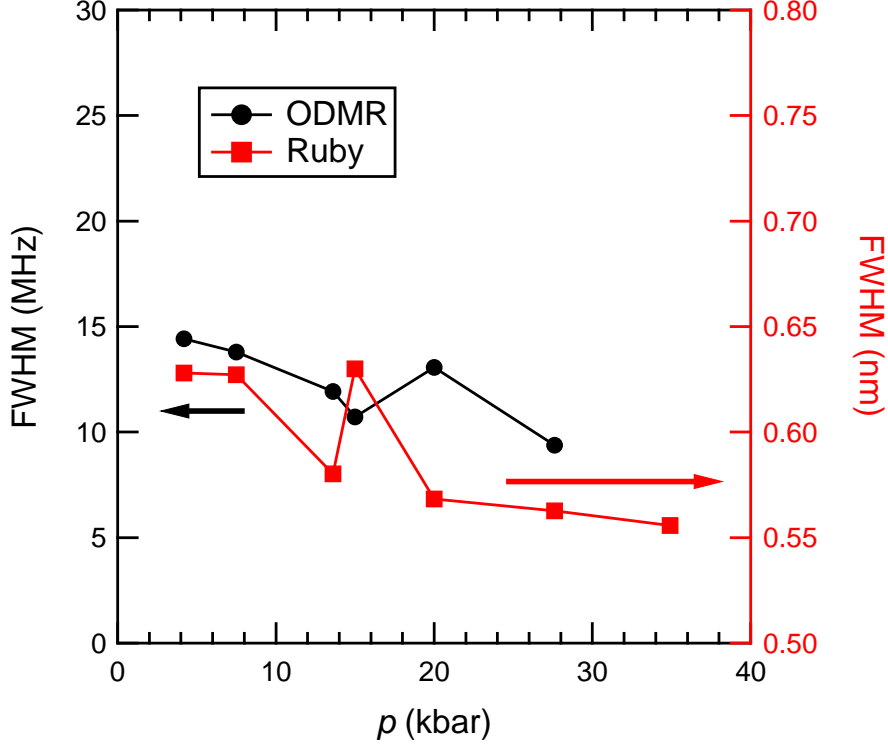


FIG. S9. Linewidth changes against pressure in both ODMR spectra (black) and spectra of ruby (red) in 99.5% pure glycerine. The ODMR spectra are taken at 30K for  $NV_C$  in the main text. The raw data of optical spectra of ruby are shown in Fig. S5.

splitting. Thus the longitudinal component of the magnetic field can be measured from the ODMR spectrum. The transverse component causes a overall frequency shift  $\Delta\varepsilon = \frac{\gamma^2(B_x^2+B_y^2)}{D}$ .

After the deduction of both temperature and pressure effects (section above), the remaining shift of the spectrum comes from the transverse component of the magnetic field. Because of the square root relationship between the field strength and the spectrum shift, the transverse field is much harder to be determined accurately, compared with the longitudinal field.

For a diamond with an ensemble of NV centers, due to four possible orientations in the diamond lattice, there can be four possible magnetic field projections, which are distinguishable in the ODMR spectrum. For each orientation, both the transverse and longitudinal components of the magnetic field can be derived from the ODMR spectra. To get the maximum sensitivity from these four possible orientations, we use the signal from the orientation

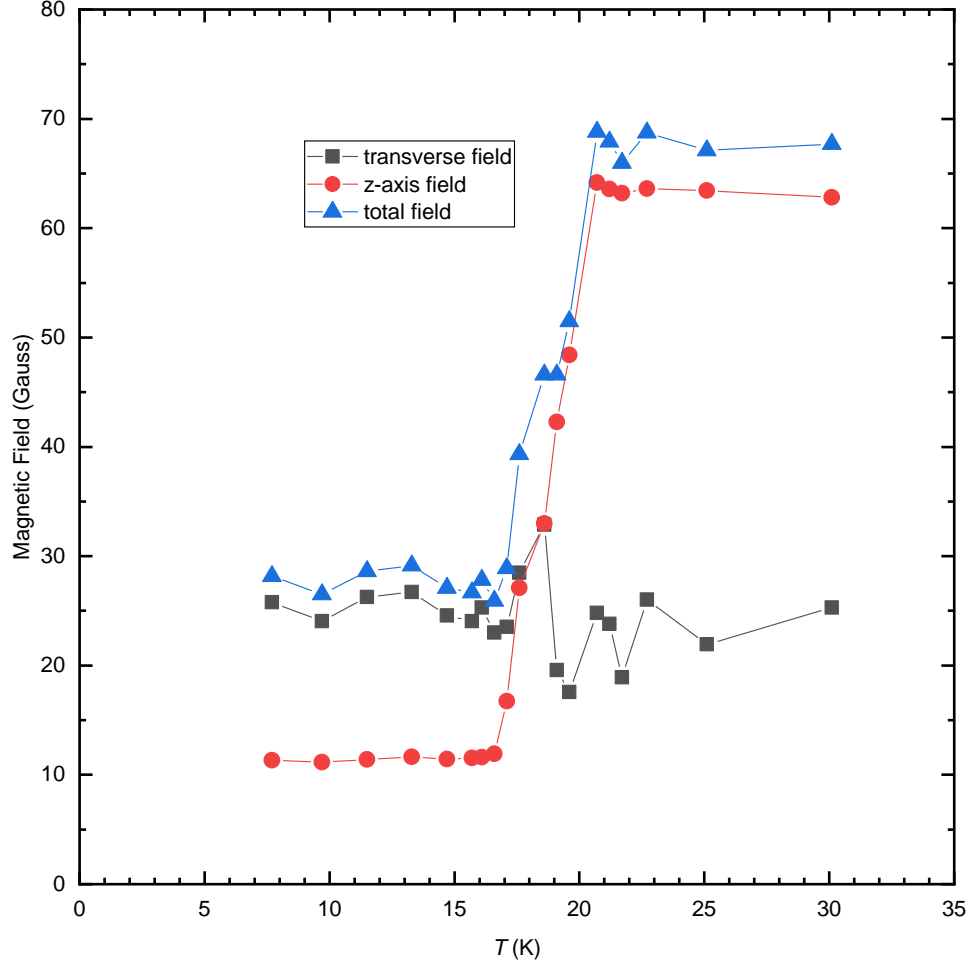


FIG. S10. **the change of longitudinal and transverse field strength of  $NV_C$  against temperature.** The pressure is 8.3 kbar.

with the largest Zeeman splitting (i.e. with the smallest transverse component) to measure the effective magnetic field strength projected on the NV center axis.

The center frequencies of the two peaks farthest apart in the ODMR spectra are determined by fitting the curves with the Lorentzian shape (see Figure 2 (B,C,D) of the main text). Both the transverse and longitudinal components are derived from these two frequencies. Fig. S10, S11, S12 show the change of magnetic fields against temperature for



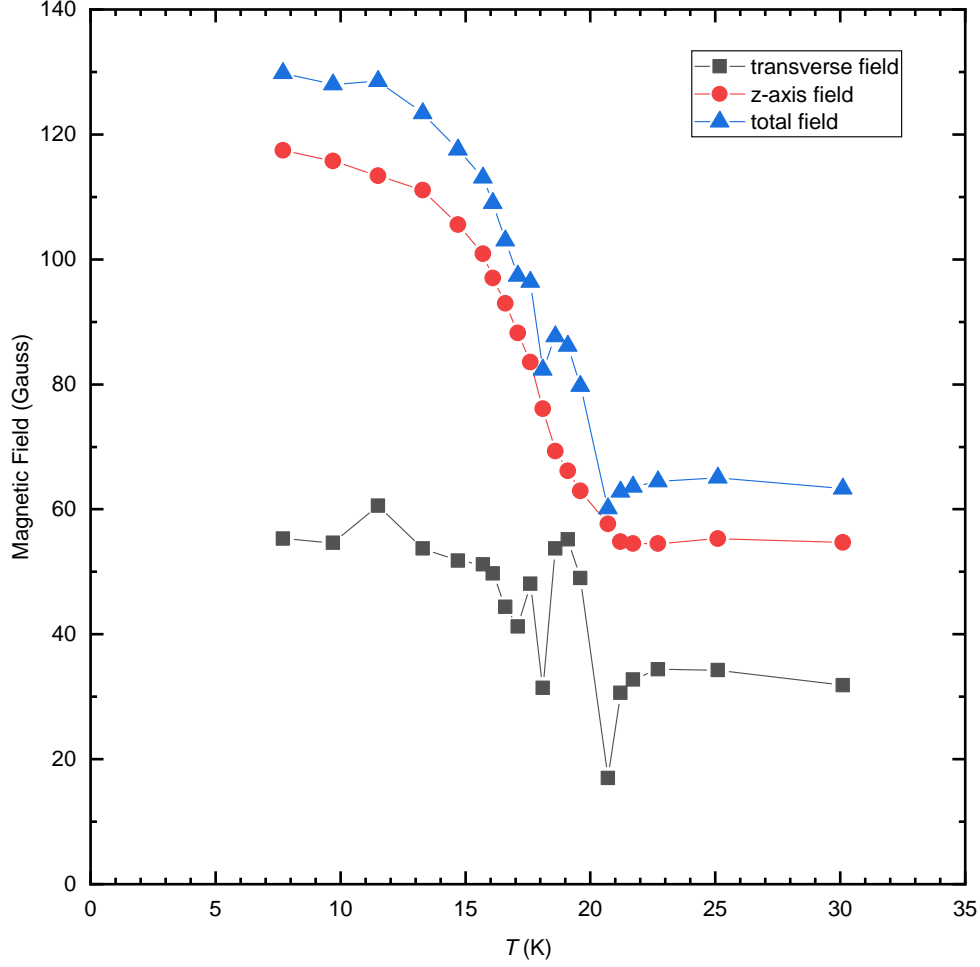


FIG. S11. **the change of longitudinal and transverse field strength of  $NV_E$  against temperature.** The pressure is 8.3 kbar.

diamond particles  $NV_C$ ,  $NV_E$ ,  $NV_F$ . The calculated transverse fields in the lower temperature range in Fig. S10 show strong fluctuations. This is because when the longitudinal field strength is small, spectrum lines from four axis partially overlapped. It is difficult to isolate the spectrum of preferred orientation by fitting. Additionally, because of the square root relationship between the field strength and spectra shift from equation (3), the uncertainty of transverse field derived from this fitting is even bigger. Overall, it is hard to derive the

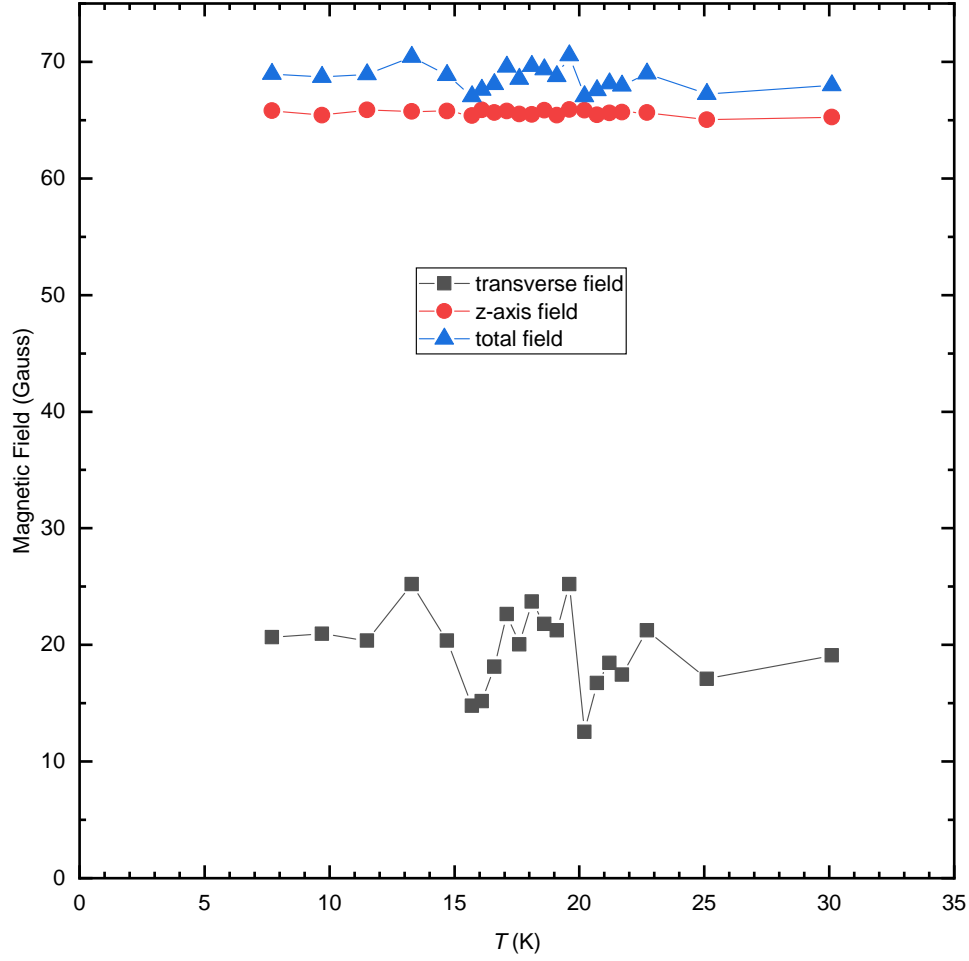


FIG. S12. the change of longitudinal and transverse field strength of  $NV_F$  against temperature. The pressure is 8.3 kbar.

transverse fields with the same accuracy as the longitudinal fields. Since the magnitude of transverse component of these three diamond particles are small and does not change much compared with longitudinal components, in the main text, we use the longitudinal components to demonstrate the diamagnetism associated with superconductivity.

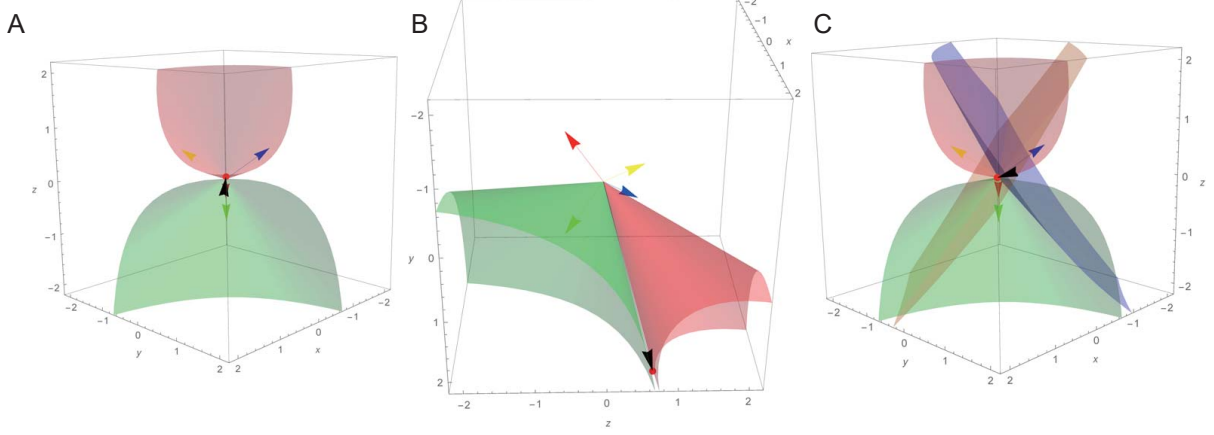


FIG. S13. **A** The front view of the two-cone method at 30 K. **B** The side view of two-cone method. **C** The four-cone method, which is in good agreement with the two-cone approximation except for a slight deviation due to the fitting and experimental errors.

## 2. Determine the magnetic field relative to the sample $c$ -axis

The diamond particles we used contain an ensemble of NV centers, which have 4 relative crystalline orientations defined by the following unit vectors,

$$\frac{1}{\sqrt{3}}[-1, -1, -1], \frac{1}{\sqrt{3}}[1, 1, -1], \frac{1}{\sqrt{3}}[-1, 1, 1], \frac{1}{\sqrt{3}}[1, -1, 1]$$

When an external static magnetic field is applied, we can observe four pairs of peaks corresponding to these four relative NV center axes. As shown above, by using the second order perturbation theory calculations stated in Ref. [37], we can deduce the relative angle between the magnetic field and any one of these four NV center axes. Now, by drawing cones about the NV axes with the deduced angles using the outermost two pairs of peaks, we can obtain a small overlapped region between these two cones, which indicates the magnetic field direction (Fig. S13A,B). If we use the remaining two orientations to draw two additional cones, they will only re-affirm the result of the pre-selected two cones with no extra information gained concerning the field profile, which is illustrated in Fig. S13C.

At 30 K, the sample is at the normal state where the magnetic field can fully penetrate the sample. The magnetic field vector  $\vec{H}(30 \text{ K})$  sensed by the diamond particle is parallel to the sample  $c$ -axis. We can observe the relative angle change of the field vector  $\vec{H}$  with respect to the sample  $c$ -axis when the sample undergoes the superconducting transition.

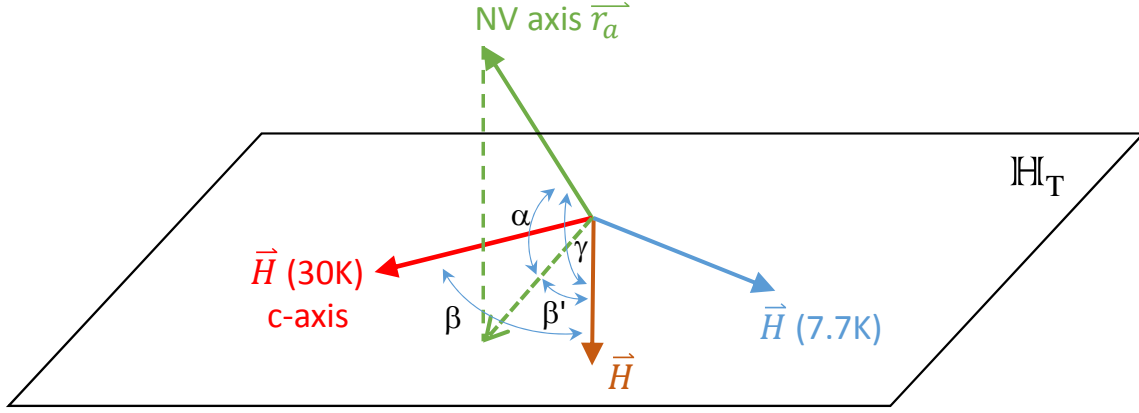


FIG. S14. Definition of various angles relative to  $\mathbb{H}_T$  plane (see text). The NV axis shown is  $\vec{r}_a$ .

We select two of four possible NV center axes to perform the two-cone method as stated above. Here we denote the selected NV center axes as  $\vec{r}_a$  and  $\vec{r}_b$  and their corresponding angles to the field vector  $\vec{H}$  as  $\theta_{small}$  and  $\theta_{large}$ , respectively. For the two-cone method, we draw a cone about  $\vec{r}_a$  using the smaller angle  $\theta_{small}$ , then we draw another cone about  $\vec{r}_b$  using the larger angle  $\theta_{large}$ . It is crucial to keep this combination fixed when we calculate the relative angle  $\beta$  between the sample  $c$ -axis and the field vector  $\vec{H}$  throughout the transition for a valid comparison. Our two-cone analysis shows that  $\vec{H}$  varies in a plane as temperature changes. To find the angle  $\beta$ , we go through the following steps.

First, we define a common plane  $\mathbb{H}_T$  in which the field vector  $\vec{H}$  varies. Second, we introduce  $\alpha$  as the angle between  $\vec{r}_a$  and  $\mathbb{H}_T$ ;  $\beta'$  is the angle between  $\vec{H}$  and the projection of  $\vec{r}_a$  on  $\mathbb{H}_T$ ;  $\gamma$  is the angle between  $\vec{r}_a$  and the field vector  $\vec{H}$ . These angles are shown in Fig. S14 and they satisfy the relationship

$$(\cos \alpha)(\cos \beta') = \cos \gamma. \quad (\text{S4})$$

For the diamond particle  $\text{NV}_C$ , within the measurement accuracy,  $\vec{r}_a$  happens to lie very close to  $\mathbb{H}_T$ , thus  $\alpha \approx 0$ , and Eq. (4) reduced to  $\cos \beta' = \cos \gamma$ . In this case, we have  $\beta = \beta' \pm \beta'(30 \text{ K})$ , where the plus or minus sign here states that if the field vector  $\vec{H}$  crosses  $\vec{r}_a$  when going from  $T < 30 \text{ K}$  to  $T = 30 \text{ K}$ , then  $\beta = \beta' + \beta'(30 \text{ K})$ . If  $\vec{H}$  does not crosses  $\vec{r}_a$ , then  $\beta = \beta' - \beta'(30 \text{ K})$ . We can see that in Fig. S15A,  $\vec{r}_a$  indicated as the black arrow is located somewhere between the red and blue arrows, and hence when the temperature

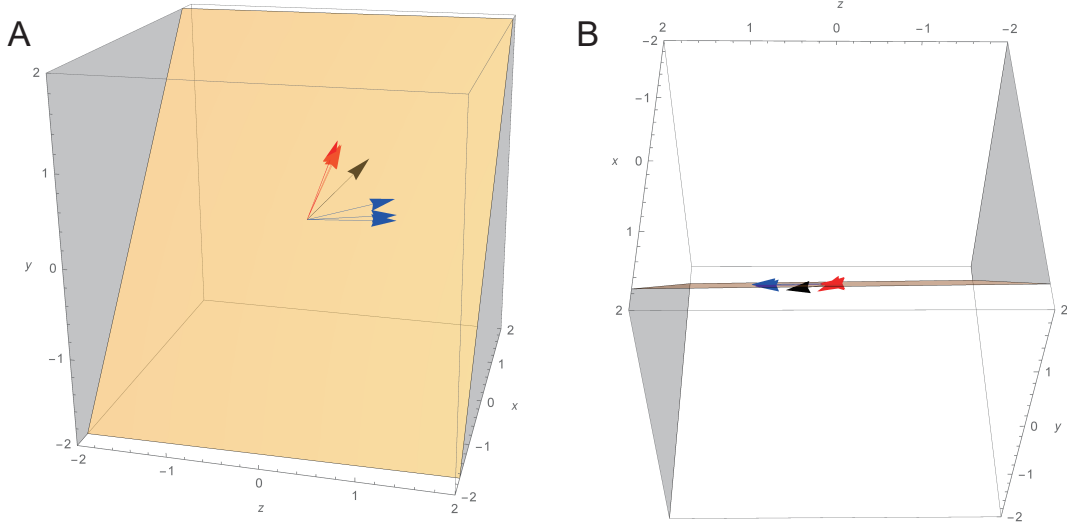


FIG. S15. **A** The red arrows indicate the field vectors at normal state, where the blue arrows indicate the vectors at the vortex and the Meissner state, the black arrow indicates the NV axis we used for the angle calculations. Yellow plane is  $\mathbb{H}_T$ . **B** Top view of the plot.

increases, the field vector  $\vec{H}$  will eventually cross  $\vec{r}_a$ , which gives rise to a sign change, as  $\gamma$  only shows the angle between  $\vec{r}_a$  and  $\vec{H}$  but not  $\vec{H}(30\text{ K})$  and  $\vec{H}$ . From this analysis, we obtain the relative angle between the magnetic field and  $c$ -axis which was shown in Fig. 2H in the main text.

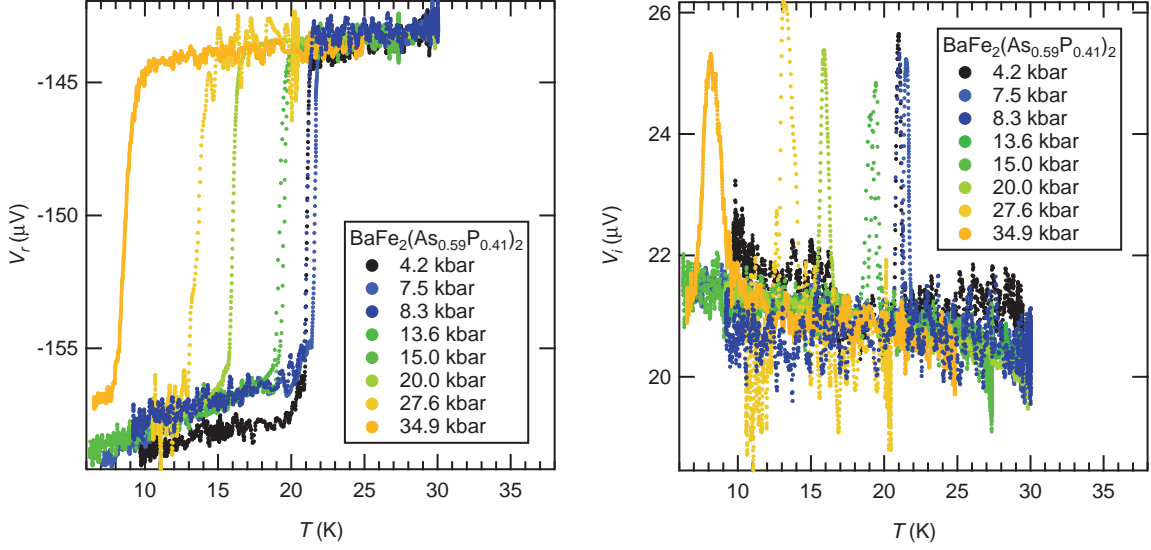


FIG. S16. The pressure dependence of the superconducting transition for  $\text{BaFe}_2(\text{As}_{0.59}\text{P}_{0.41})_2$  measured by the AC susceptibility measurements. The left (right) panel shows the real (imaginary) part of the pick-up voltage.

### 3. AC SUSCEPTIBILITY MEASUREMENTS

To construct the  $T - p$  phase diagram of  $\text{BaFe}_2(\text{As}_{0.59}\text{P}_{0.41})_2$  (Fig. 3B of the main text), AC susceptibility measurements have been performed as a supplementary method to track the evolution of  $T_c$  under pressure, in addition to the ODMR measurement. This method has been shown to successfully capture the superconducting transition in this class of materials under pressure [25]. Hence it is valid to implement this technique in our experiment as the benchmarking method. The outer modulation coil provides an AC modulation field of  $\sim 1$  G while the inner microcoil serves as a signal pickup coil (See Fig. 1A of the main text and Fig. S3A of SM). Fig. S16 shows the experimental data collected by the AC susceptibility measurement. The left (right) panel shows the real (imaginary) part of the pick-up voltage. The  $T_c$  values in Fig. 3B are determined by the peaks in the imaginary part of the pick-up voltage.

#### 4. OPTIMIZING THE ODMR PULSE SEQUENCE BY EXAMINING THE THERMAL LOAD FROM THE MEASUREMENTS

Superconductivity is sensitive to temperature, particularly near the phase boundary. Our ODMR measurement protocol requires the use of both laser excitation and microwave excitation, which could lead to the heating of the sample.

To investigate the laser heating effect, we use  $T_c$  measured by AC susceptibility as a benchmark. We conducted a series of AC susceptibility measurements with the laser power increased from 0 to 1 mW. We have not detected any change of  $T_c$ . Note that the laser power we used in the experiments (7  $\mu$ W to 15  $\mu$ W) was much lower than 1 mW. Therefore, we conclude that there is no laser heating in this experiment.

Next, we investigate the possible heating effect from the microwave. The power of the microwave sent into the cryostat is around 30 mW, which is much smaller than the nominal cooling power of the cryostat at 10 K (1 W) at the sample position. However, the local heating could still be possible due to the limited thermal conductivity. To check if there is a heating effect that can influence our experimental observations, we performed the ODMR measurements on NV<sub>C</sub> with different duty cycles (shown schematically in the insert of Fig. S17): 1. CW measurement with no wait time ( $t_{wait} = 0$ ), data shown as red circles in Fig. S17; 2. pulsed measurement with  $t_{wait} = 2000$  ns and  $t_{laser} = 1000$  ns, data shown as blue squares; 3. pulsed measurement with  $t_{wait} = 5000$  ns and  $t_{laser} = 1000$  ns, data shown as green triangles. There is no observable difference among these curves. Since vortex states are sensitive to temperature changes, our experiment shows there is no noticeable heating effect even with the CW ODMR method. This exercise also shows the good reproducibility of the ODMR protocol in general.

For experiments shown in the main text, the pulse sequences is either with  $t_{wait} = 2000$  ns (Figure 2 and 3) or with  $t_{wait} = 4000$  ns (Figure 4). In both cases,  $t_{laser} = 1000$  ns. These values are chosen to strike a good balance: the possibility of heating is minimized, while the measurement time does not become too long.

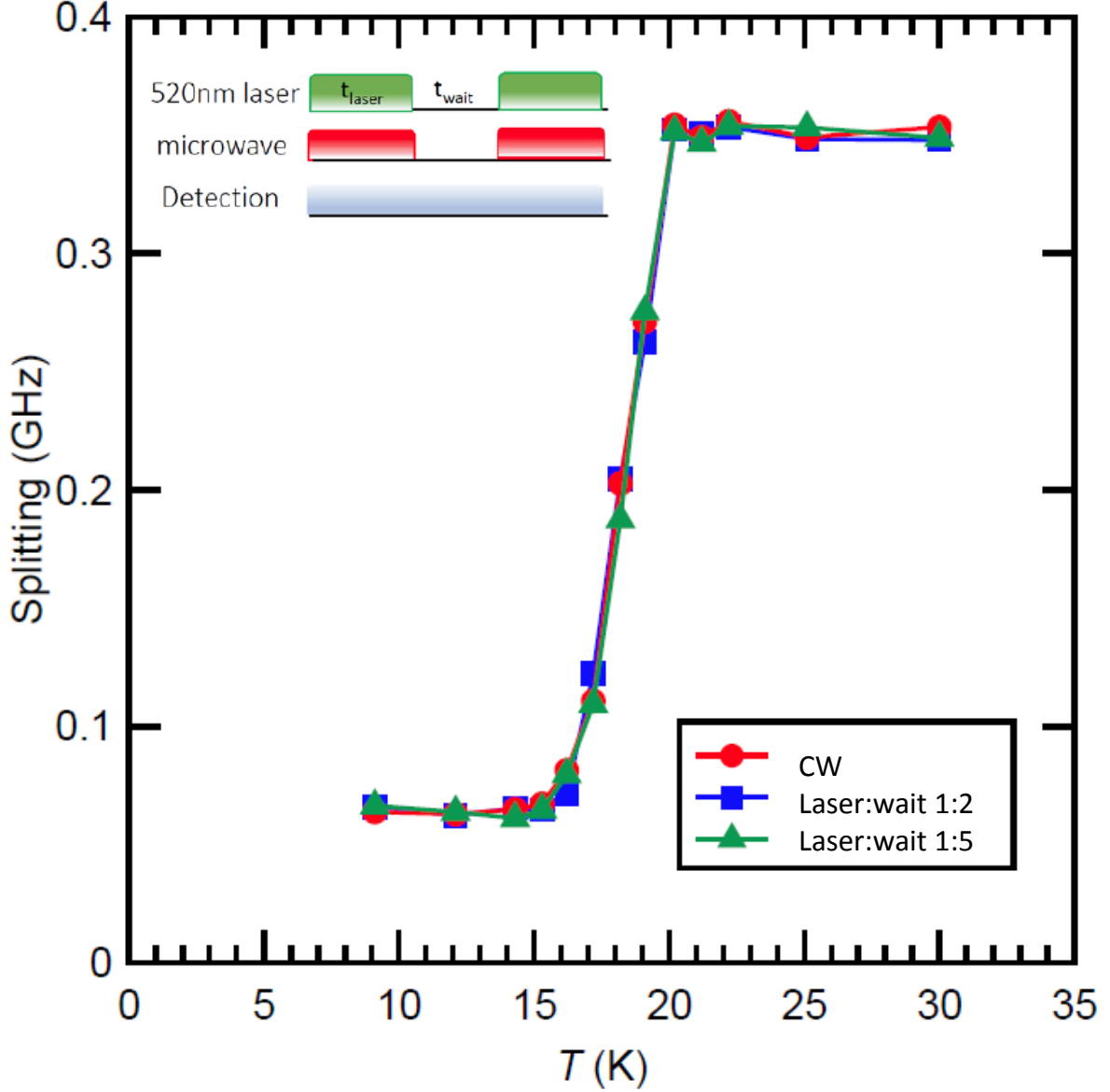


FIG. S17. The diamagnetism associated with superconductivity measured by the ODMR method with different duty cycles for NV<sub>C</sub>. (Inset), the pulse sequence.

## 5. THE DIAMAGNETISM ASSOCIATED WITH SUPERCONDUCTIVITY MEASURED VIA NANODIAMONDS

As discussed in Section 1C, the spatial resolution can be improved by using smaller particles. In the study shown in the main text, we have used diamond particles with an average size of 1  $\mu\text{m}$ . In this section, we present some preliminary data showing the observation of the diamagnetism associated with superconductivity with nanodiamonds of an average



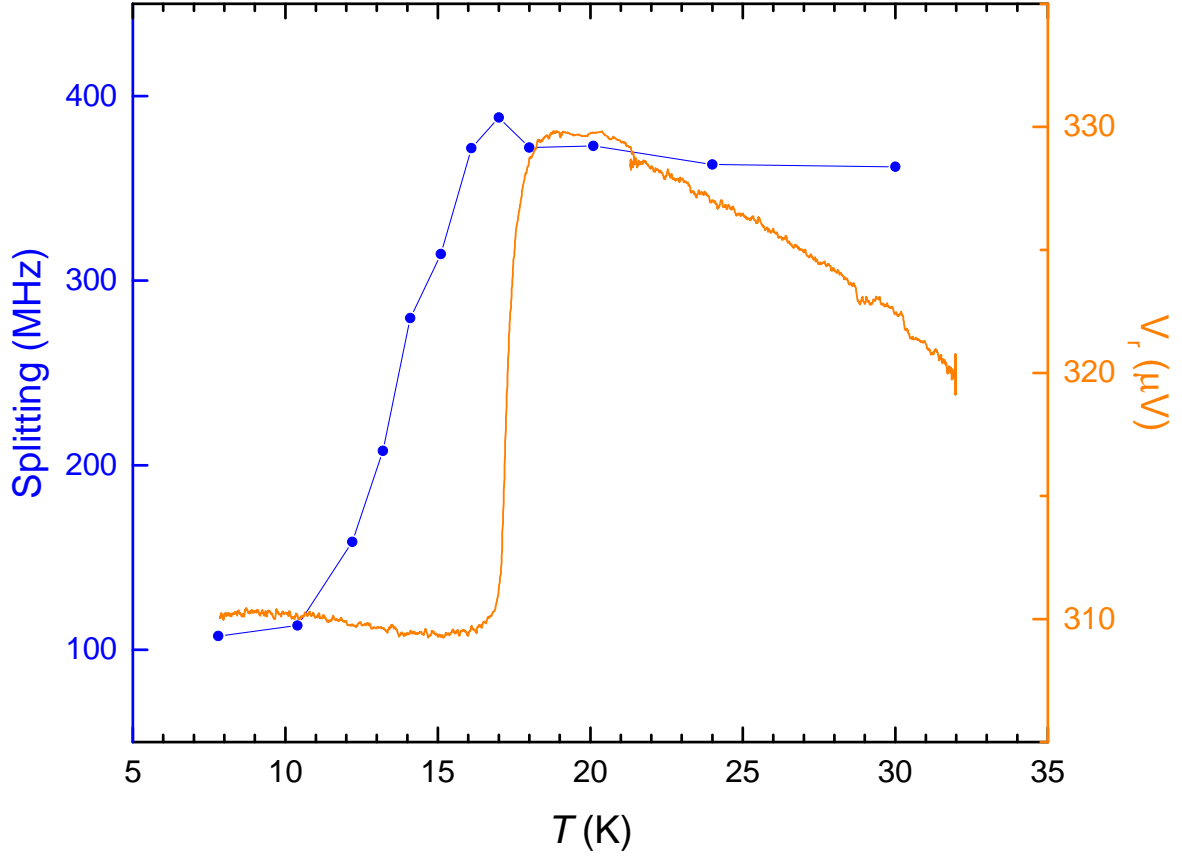


FIG. S18. The diamagnetism associated with superconductivity measured via NV centers inside 140 nm size nanodiamonds. The applied pressure is 18 kbar.

size around 140 nm. The number of NV centers per particle is around 1200. We used the same pressure cell design, the same type of sample and the same experimental protocol. Fig. S18 shows the diamagnetism associated with superconductivity of  $\text{BaFe}_2(\text{As}_{0.59}\text{P}_{0.41})_2$  sample at 18 kbar. The results are similar to what we observed with the micron-sized diamond particles in the main text (Fig. 3A). This shows the potential of reaching 100 nm spatial resolution with this protocol. Since the particles are smaller than the vortex lattice constant  $a_V$ , the dynamics of individual vortices can potentially be studied, although more sophisticated analysis and experimental protocol are needed.

## 6. DETERMINING THE AMBIENT PRESSURE $T_c$ VIA AC SUSCEPTIBILITY AND RESISTIVITY MEASUREMENTS

To obtain the ambient pressure  $T_c$  of  $\text{BaFe}_2(\text{As}_{0.59}\text{P}_{0.41})_2$  shown in Figure 3B of the main text, AC susceptibility and resistivity measurements have been performed simultaneously on another piece of crystal from the same batch. The dimensions of this sample are shown in Table S1. In the resistivity measurement,  $T_c$  is defined as the temperature when the resistivity reaches zero. In the AC susceptibility measurement,  $T_c$  is defined as the temperature corresponding to the peak of the imaginary part. During the superconducting transition, the superconductor enters the Meissner state, a large change in the real part can be used to identify the appearance of superconductivity. The imaginary part is suitable for determining the  $T_c$  as its peak is significant to pinpoint the transition. In Figure S19, both the AC susceptibility and resistivity measurements show a similar sharp transition around  $T_c$ . All data presented in Figure S19 were collected on warming up, while a similar set of data were collected on cooling down (not shown). Table S2 summarizes the  $T_c$ , obtained by taking the average of the respective values extracted from the cooldown and the warm-up data. The values are in agreement with the previously reported value [22].

TABLE S1. Dimensions of the sample using in this measurement

Effective length (cm)	$3.89 \times 10^{-3}$
Cross section area ( $\text{cm}^2$ )	$1.66 \times 10^{-4}$

TABLE S2.  $T_c$  obtained from the AC susceptibility and resistivity measurements (average value of data from cooldown and warm-up sweeps)

	$T_c$ (K)
AC susceptibility	23.5
Resistivity	23.8

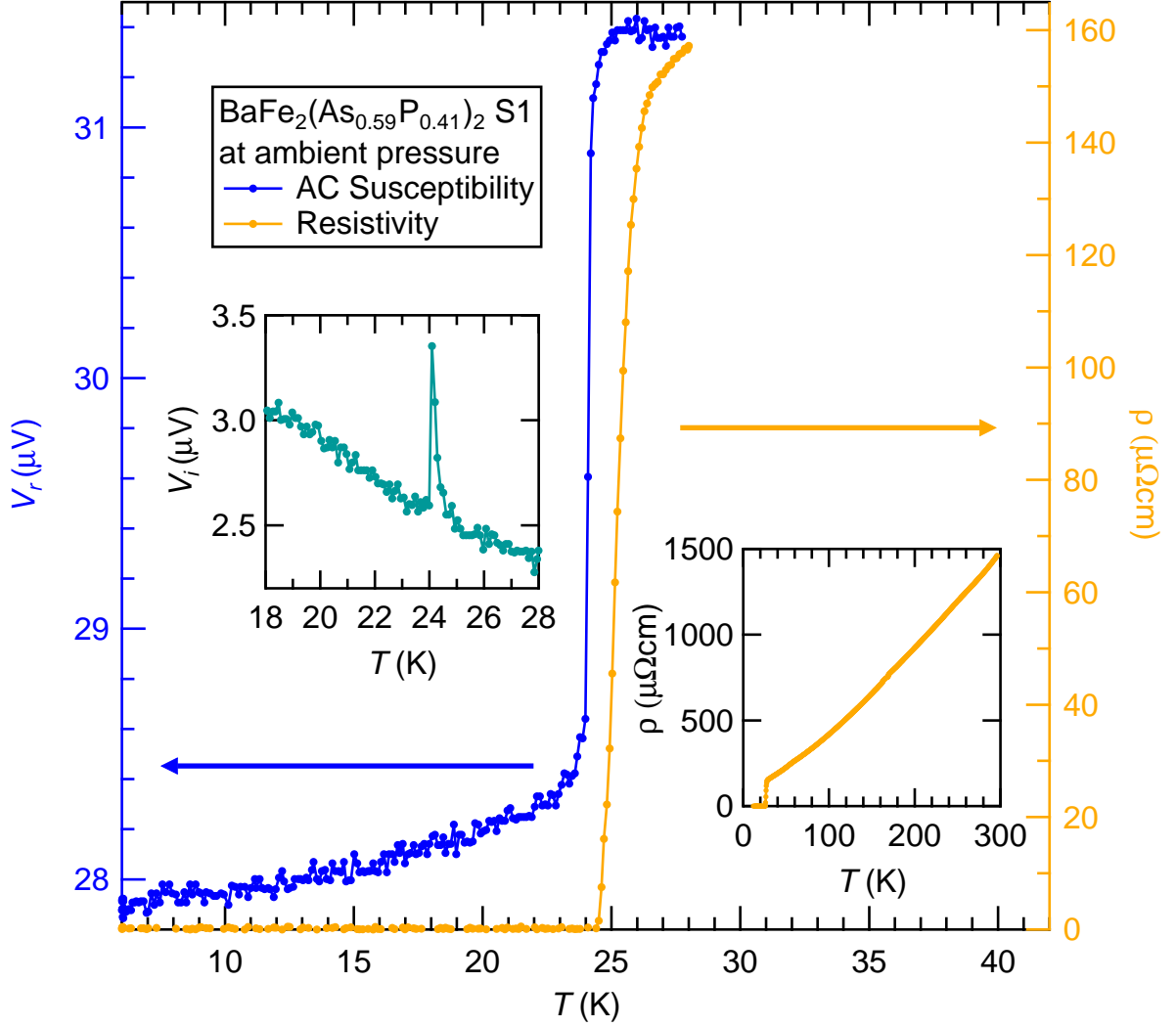


FIG. S19. AC susceptibility and resistivity data of BaFe<sub>2</sub>(As<sub>0.59</sub>P<sub>0.41</sub>)<sub>2</sub>. Insets: (left) imaginary part of AC susceptibility, and (right) resistivity from base temperature to 300 K. All data presented in this figure were collected on warming up.

## References and Notes

1. M. Tinkham, *Introduction to Superconductivity* (McGraw-Hill, ed. 2, 1996).
2. N. D. Mathur, F. M. Grosche, S. R. Julian, I. R. Walker, D. M. Freye, R. K. W. Haselwimmer, G. G. Lonzarich, Magnetically mediated superconductivity in heavy fermion compounds. *Nature* **394**, 39–43 (1998). [doi:10.1038/27838](https://doi.org/10.1038/27838)
3. S. S. Saxena, P. Agarwal, K. Ahilan, F. M. Grosche, R. K. W. Haselwimmer, M. J. Steiner, E. Pugh, I. R. Walker, S. R. Julian, P. Monthoux, G. G. Lonzarich, A. Huxley, I. Sheikin, D. Braithwaite, J. Flouquet, Superconductivity on the border of itinerant-electron ferromagnetism in UGe<sub>2</sub>. *Nature* **406**, 587–592 (2000). [doi:10.1038/35020500](https://doi.org/10.1038/35020500) [Medline](#)
4. S. K. Goh, D. A. Tompsett, P. J. Saines, H. C. Chang, T. Matsumoto, M. Imai, K. Yoshimura, F. M. Grosche, Ambient pressure structural quantum critical point in the phase diagram of (Ca<sub>x</sub>Sr<sub>1-x</sub>)<sub>3</sub>Rh<sub>4</sub>Sn<sub>13</sub>. *Phys. Rev. Lett.* **114**, 097002 (2015). [doi:10.1103/PhysRevLett.114.097002](https://doi.org/10.1103/PhysRevLett.114.097002) [Medline](#)
5. S. Hosoi, K. Matsuura, K. Ishida, H. Wang, Y. Mizukami, T. Watashige, S. Kasahara, Y. Matsuda, T. Shibauchi, Nematic quantum critical point without magnetism in FeSe<sub>1-x</sub>S<sub>x</sub> superconductors. *Proc. Natl. Acad. Sci. U.S.A.* **113**, 8139–8143 (2016). [doi:10.1073/pnas.1605806113](https://doi.org/10.1073/pnas.1605806113) [Medline](#)
6. J. Paglione, R. L. Greene, High-temperature superconductivity in iron-based materials. *Nat. Phys.* **6**, 645–658 (2010). [doi:10.1038/nphys1759](https://doi.org/10.1038/nphys1759)
7. M. Somayazulu, M. Ahart, A. K. Mishra, Z. M. Geballe, M. Baldini, Y. Meng, V. V. Struzhkin, R. J. Hemley, Evidence for superconductivity above 260 K in lanthanum superhydride at megabar pressures. *Phys. Rev. Lett.* **122**, 027001 (2019). [doi:10.1103/PhysRevLett.122.027001](https://doi.org/10.1103/PhysRevLett.122.027001) [Medline](#)
8. A. P. Drozdov, P. P. Kong, V. S. Minkov, S. P. Besedin, M. A. Kuzovnikov, S. Mozaffari, L. Balicas, F. F. Balakirev, D. E. Graf, V. B. Prakapenka, E. Greenberg, D. A. Knyazev, M. Tkacz, M. I. Erements, Superconductivity at 250 K in lanthanum hydride under high pressures. *Nature* **569**, 528–531 (2019). [doi:10.1038/s41586-019-1201-8](https://doi.org/10.1038/s41586-019-1201-8) [Medline](#)
9. F. Jelezko, J. Wrachtrup, Single defect centres in diamond: A review. *Phys. Status Solidi* **203**, 3207–3225 (2006) (a). [doi:10.1002/pssa.200671403](https://doi.org/10.1002/pssa.200671403)
10. M. W. Doherty, N. B. Manson, P. Delaney, F. Jelezko, J. Wrachtrup, L. C. L. Hollenberg, The nitrogen-vacancy colour centre in diamond. *Phys. Rep.* **528**, 1–45 (2013). [doi:10.1016/j.physrep.2013.02.001](https://doi.org/10.1016/j.physrep.2013.02.001)
11. G. Balasubramanian, I. Y. Chan, R. Kolesov, M. Al-Hmoud, J. Tisler, C. Shin, C. Kim, A. Wojcik, P. R. Hemmer, A. Krueger, T. Hanke, A. Leitenstorfer, R. Bratschitsch, F. Jelezko, J. Wrachtrup, Nanoscale imaging magnetometry with diamond spins under ambient conditions. *Nature* **455**, 648–651 (2008). [doi:10.1038/nature07278](https://doi.org/10.1038/nature07278) [Medline](#)
12. J. R. Maze, P. L. Stanwix, J. S. Hodges, S. Hong, J. M. Taylor, P. Cappellaro, L. Jiang, M. V. G. Dutt, E. Togan, A. S. Zibrov, A. Yacoby, R. L. Walsworth, M. D. Lukin, Nanoscale magnetic sensing with an individual electronic spin in diamond. *Nature* **455**, 644–647 (2008). [doi:10.1038/nature07279](https://doi.org/10.1038/nature07279) [Medline](#)

13. L. Rondin, J.-P. Tetienne, T. Hingant, J.-F. Roch, P. Maletinsky, V. Jacques, Magnetometry with nitrogen-vacancy defects in diamond. *Rep. Prog. Phys.* **77**, 056503 (2014). [doi:10.1088/0034-4885/77/5/056503](https://doi.org/10.1088/0034-4885/77/5/056503) [Medline](#)
14. P. Neumann, I. Jakobi, F. Dolde, C. Burk, R. Reuter, G. Waldherr, J. Honert, T. Wolf, A. Brunner, J. H. Shim, D. Suter, H. Sumiya, J. Isoya, J. Wrachtrup, High-precision nanoscale temperature sensing using single defects in diamond. *Nano Lett.* **13**, 2738–2742 (2013). [doi:10.1021/nl401216y](https://doi.org/10.1021/nl401216y) [Medline](#)
15. G. Kucsko, P. C. Maurer, N. Y. Yao, M. Kubo, H. J. Noh, P. K. Lo, H. Park, M. D. Lukin, Nanometre-scale thermometry in a living cell. *Nature* **500**, 54–58 (2013). [doi:10.1038/nature12373](https://doi.org/10.1038/nature12373) [Medline](#)
16. M. W. Doherty, V. V. Struzhkin, D. A. Simpson, L. P. McGuinness, Y. Meng, A. Stacey, T. J. Karle, R. J. Hemley, N. B. Manson, L. C. L. Hollenberg, S. Prawer, Electronic properties and metrology applications of the diamond NV- center under pressure. *Phys. Rev. Lett.* **112**, 047601 (2014). [doi:10.1103/PhysRevLett.112.047601](https://doi.org/10.1103/PhysRevLett.112.047601) [Medline](#)
17. A. Waxman, Y. Schlussel, D. Groswasser, V. M. Acosta, L.-S. Bouchard, D. Budker, R. Folman, Diamond magnetometry of superconducting thin films. *Phys. Rev. B Condens. Matter Mater. Phys.* **89**, 054509 (2014). [doi:10.1103/PhysRevB.89.054509](https://doi.org/10.1103/PhysRevB.89.054509)
18. N. M. Nusran, K. R. Joshi, K. Cho, M. A. Tanatar, W. R. Meier, S. L. Bud'ko, P. C. Canfield, Y. Liu, T. A. Lograsso, R. Prozorov, Spatially-resolved study of the Meissner effect in superconductors using NV-centers-in-diamond optical magnetometry. *New J. Phys.* **20**, 043010 (2018). [doi:10.1088/1367-2630/aab47c](https://doi.org/10.1088/1367-2630/aab47c)
19. K. Joshi, N. M. Nusran, M. A. Tanatar, K. Cho, W. R. Meier, S. L. Bud'ko, P. C. Canfield, R. Prozorov, Measuring the lower critical field of superconductors using nitrogen-vacancy centers in diamond optical magnetometry. *Phys. Rev. Appl.* **11**, 014035 (2019). [doi:10.1103/PhysRevApplied.11.014035](https://doi.org/10.1103/PhysRevApplied.11.014035)
20. Materials and methods are available as supplementary materials.
21. L. Steele, M. Lawson, M. Onyszcak, B. T. Bush, Z. Mei, A. P. Dioguardi, J. King, A. Parker, A. Pines, S. T. Weir, W. Evans, K. Visbeck, Y. K. Vohra, N. J. Curro, Optically detected magnetic resonance of nitrogen vacancies in a diamond anvil cell using designer diamond anvils. *Appl. Phys. Lett.* **111**, 221903 (2017). [doi:10.1063/1.5004153](https://doi.org/10.1063/1.5004153)
22. S. Kasahara, T. Shibauchi, K. Hashimoto, K. Ikada, S. Tonegawa, R. Okazaki, H. Shishido, H. Ikeda, H. Takeya, K. Hirata, T. Terashima, Y. Matsuda, Evolution from non-Fermi- to Fermi-liquid transport via isovalent doping in  $\text{BaFe}_2(\text{As}_{1-x}\text{P}_x)_2$  superconductors. *Phys. Rev. B Condens. Matter Mater. Phys.* **81**, 184519 (2010). [doi:10.1103/PhysRevB.81.184519](https://doi.org/10.1103/PhysRevB.81.184519)
23. K. Hashimoto, K. Cho, T. Shibauchi, S. Kasahara, Y. Mizukami, R. Katsumata, Y. Tsuruhara, T. Terashima, H. Ikeda, M. A. Tanatar, H. Kitano, N. Salovich, R. W. Giannetta, P. Walmsley, A. Carrington, R. Prozorov, Y. Matsuda, A sharp peak of the zero-temperature penetration depth at optimal composition in  $\text{BaFe}_2(\text{As}_{1-x}\text{P}_x)_2$ . *Science* **336**, 1554–1557 (2012). [doi:10.1126/science.1219821](https://doi.org/10.1126/science.1219821) [Medline](#)

24. T. Shibauchi, A. Carrington, Y. Matsuda, A quantum critical point lying beneath the superconducting dome in iron pnictides. *Annu. Rev. Condens. Matter Phys.* **5**, 113–135 (2014). [doi:10.1146/annurev-conmatphys-031113-133921](https://doi.org/10.1146/annurev-conmatphys-031113-133921)
25. L. E. Klintberg, S. K. Goh, S. Kasahara, Y. Nakai, K. Ishida, M. Sutherland, T. Shibauchi, Y. Matsuda, T. Terashima, Chemical pressure and physical pressure in  $\text{BaFe}_2(\text{As}_{1-x}\text{P}_x)_2$ . *J. Phys. Soc. Jpn.* **79**, 123706 (2010). [doi:10.1143/JPSJ.79.123706](https://doi.org/10.1143/JPSJ.79.123706)
26. K. Y. Yip, Y. C. Chan, Q. Niu, K. Matsuura, Y. Mizukami, S. Kasahara, Y. Matsuda, T. Shibauchi, S. K. Goh, Weakening of the diamagnetic shielding in  $\text{FeSe}_{1-x}\text{S}_x$  at high pressures. *Phys. Rev. B* **96**, 020502 (2017). [doi:10.1103/PhysRevB.96.020502](https://doi.org/10.1103/PhysRevB.96.020502)
27. C. Putzke, P. Walmsley, J. D. Fletcher, L. Malone, D. Vignolles, C. Proust, S. Badoux, P. See, H. E. Beere, D. A. Ritchie, S. Kasahara, Y. Mizukami, T. Shibauchi, Y. Matsuda, A. Carrington, Anomalous critical fields in quantum critical superconductors. *Nat. Commun.* **5**, 5679 (2014). [doi:10.1038/ncomms6679](https://doi.org/10.1038/ncomms6679) [Medline](#)
28. Y. Lamhot, A. Yagil, N. Shapira, S. Kasahara, T. Watashige, T. Shibauchi, Y. Matsuda, O. M. Auslaender, Local characterization of superconductivity in  $\text{BaFe}_2(\text{As}_{1-x}\text{P}_x)_2$ . *Phys. Rev. B Condens. Matter Mater. Phys.* **91**, 060504 (2015). [doi:10.1103/PhysRevB.91.060504](https://doi.org/10.1103/PhysRevB.91.060504)
29. L. Rondin, J.-P. Tetienne, S. Rohart, A. Thiaville, T. Hingant, P. Spinicelli, J.-F. Roch, V. Jacques, Stray-field imaging of magnetic vortices with a single diamond spin. *Nat. Commun.* **4**, 2279 (2013). [doi:10.1038/ncomms3279](https://doi.org/10.1038/ncomms3279) [Medline](#)
30. M. Pelliccione, A. Jenkins, P. Ovartchaiyapong, C. Reetz, E. Emmanouilidou, N. Ni, A. C. Bleszynski Jayich, Scanned probe imaging of nanoscale magnetism at cryogenic temperatures with a single-spin quantum sensor. *Nat. Nanotechnol.* **11**, 700–705 (2016). [doi:10.1038/nnano.2016.68](https://doi.org/10.1038/nnano.2016.68) [Medline](#)
31. L. Thiel, D. Rohner, M. Ganzhorn, P. Appel, E. Neu, B. Müller, R. Kleiner, D. Koelle, P. Maletinsky, Quantitative nanoscale vortex imaging using a cryogenic quantum magnetometer. *Nat. Nanotechnol.* **11**, 677–681 (2016). [doi:10.1038/nnano.2016.63](https://doi.org/10.1038/nnano.2016.63) [Medline](#)
32. Y. Schlusser, T. Lenz, D. Rohner, Y. Bar-Haim, L. Bougas, D. Groswasser, M. Kieschnick, E. Rozenberg, L. Thiel, A. Waxman, J. Meijer, P. Maletinsky, D. Budker, R. Folman, Wide-field imaging of superconductor vortices with electron spins in diamond. *Phys. Rev. Appl.* **10**, 034032 (2018). [doi:10.1103/PhysRevApplied.10.034032](https://doi.org/10.1103/PhysRevApplied.10.034032)
33. Y. Cao, V. Fatemi, S. Fang, K. Watanabe, T. Taniguchi, E. Kaxiras, P. Jarillo-Herrero, Unconventional superconductivity in magic-angle graphene superlattices. *Nature* **556**, 43–50 (2018). [doi:10.1038/nature26160](https://doi.org/10.1038/nature26160) [Medline](#)
34. P. L. Alireza, S. R. Julian, Susceptibility measurements at high pressures using a microcoil system in an anvil cell. *Rev. Sci. Instrum.* **74**, 4728–4731 (2003). [doi:10.1063/1.1614861](https://doi.org/10.1063/1.1614861)
35. E. H. Brandt, Irreversible magnetization of pin-free type-II superconductors. *Phys. Rev. B Condens. Matter Mater. Phys.* **60**, 11939–11942 (1999). [doi:10.1103/PhysRevB.60.11939](https://doi.org/10.1103/PhysRevB.60.11939)

36. K. Y. Yip *et al.*, Data for Measuring magnetic field texture in correlated electron systems under extreme conditions. Zenodo (2019); doi:10.5281/zenodo.3490189
37. C. S. Shin, C. E. Avalos, M. C. Butler, H.-J. Wang, S. J. Seltzer, R.-B. Liu, A. Pines, V. S. Bajaj, Suppression of electron spin decoherence of the diamond NV center by a transverse magnetic field. *Phys. Rev. B Condens. Matter Mater. Phys.* **88**, 161412 (2013). [doi:10.1103/PhysRevB.88.161412](https://doi.org/10.1103/PhysRevB.88.161412)
38. M. W. Doherty, J. Michl, F. Dolde, I. Jakobi, P. Neumann, N. B. Manson, J. Wrachtrup, Measuring the defect structure orientation of a single NV<sup>-</sup> centre in diamond. *New J. Phys.* **16**, 063067 (2014). [doi:10.1088/1367-2630/16/6/063067](https://doi.org/10.1088/1367-2630/16/6/063067)
39. M. Eremets, *High Pressure Experimental Methods* (Oxford Univ. Press, 1996).
40. R. A. Forman, G. J. Piermarini, J. D. Barnett, S. Block, Pressure measurement made by the utilization of ruby sharp-line luminescence. *Science* **176**, 284–285 (1972). [doi:10.1126/science.176.4032.284](https://doi.org/10.1126/science.176.4032.284) [Medline](#)
41. M. W. Doherty, V. M. Acosta, A. Jarmola, M. S. J. Barson, N. B. Manson, D. Budker, L. C. L. Hollenberg, Temperature shifts of the resonances of the NV-center in diamond. *Phys. Rev. B Condens. Matter Mater. Phys.* **90**, 041201 (2014). [doi:10.1103/PhysRevB.90.041201](https://doi.org/10.1103/PhysRevB.90.041201)
42. R. J. Angel, M. Bujak, J. Zhao, G. D. Gatta, S. D. Jacobsen, Effective hydrostatic limits of pressure media for high-pressure crystallographic studies. *J. Appl. Cryst.* **40**, 26–32 (2007). [doi:10.1107/S0021889806045523](https://doi.org/10.1107/S0021889806045523)
43. T. Osakabe, K. Kakurai, Feasibility tests on pressure-transmitting media for single-crystal magnetic neutron diffraction under high pressure. *Jpn. J. Appl. Phys.* **47**, 6544–6547 (2008). [doi:10.1143/JJAP.47.6544](https://doi.org/10.1143/JJAP.47.6544)